CENTRAL ASIAN JOURNAL OF MEDICAL AND NATURAL SCIENCES
https://cajmns.centralasianstudies.org/index.php/CAJMNS
Volume: 05 Issue: 02 | April 2024 ISSN: 2660-4159

Article

Examines Both Structural Optimization and Spectroscopic Analysis of $C_{16}H_{13}N_3O$ and its Brominated and Chlorinated Derivative Compounds Through Infrared and Ultraviolet-Visible Spectroscopy Techniques.

Zahraa Tileb Ghaleb*[1], Naglaa Jalil Khalil[2], Nashwan Omar Tapabashi[3]

[1,2,3]Department of Chemistry, College of Sciences, University of Kirkuk, Kirkuk, Iraq
* Correspondence: zahra@uokirkuk.edu.iq

Citation: Ghaleb Z. T., Khalil N. J., Tapabashi N. O. Examines Both Structural Optimization and Spectroscopic Analysis of $C_{16}H_{13}N_3O$ and its Brominated and Chlorinated Derivative Compounds Through Infrared and Ultraviolet-Visible Spectroscopy Techniques. Central Asian Journal of Medical and Natural Science 2026, 7(2), 301–323.

Received: 12th Feb 2026
Revised: 22th Feb 2026
Accepted: 28th Feb 2026
Published: 3th Mar 2026

Copyright: © 2026 by the authors. Submitted for open access publication under the terms and conditions of the Creative Commons Attribution (CC BY) license (https://creativecommons.org/licenses/by/4.0/)

Abstract: The investigation combines theoretical research with practical testing to analyze the indole-based hydrazone derivatives A1 A2 and A3. The researchers achieved successful compound creation through condensation reactions which produced crystalline solids in high yield. We conducted our research by using DFT calculations together with experimental spectroscopy methods to study the molecular structures and physicochemical properties of the compounds. The DFT/B3LYP level required geometry optimizations to use both the STO-3G* and 3-21G basis sets for its calculations. The optimization process created stable structures which sustained their most stable state throughout the entire evaluation period. The 3-21G basis set produced bond lengths which were shorter and bond angles which reached higher accuracy compared to the STO-3G*. The method provides improved accuracy for both electron delocalization and molecular polarization effects according to this result. Heteroatom bonds with halogen substituents showed more pronounced bond length measurement differences during analysis. The halogenated compounds A2 and A3 exhibit lengthened C–Br and C–Cl bonds because additional halogen elements produce stronger polarizing effects. The optimized geometries showed systems which maintained their near-planar structure because their π-electron system extended over a wider area. The Mulliken population analysis showed a strong relationship between the analysis results and the basis-set size of the study. The negative charges of nitrogen and oxygen atoms reached their maximum strength because the atoms held their lone pairs in fixed positions. Bromine substitution caused a greater increase in electronic polarization than chlorine substitution did. The calculated vibrational frequencies showed strong similarity to the results of experimental FT-IR spectroscopy analysis. The study demonstrates that the combination of experimental methods with DFT calculations delivers precise structural and spectroscopic data for the tested compounds.

Keywords: $C_{16}H_{13}N_3O$ $C_{16}H_{12}BrN_3O$ and $C_{16}H_{12}ClN_3O$, structural properties ,DFT FT-IR and TD-DFT UV-Vis techniques.

1. Introduction

Pregnancy loss is described as the natural termination of a pregnancy prior to the viability of a fetus; it includes all losses from conception up to 20-24 weeks of pregnancy. On the other hand, the term 'miscarriage' refers to the loss of an intrauterine pregnancy IUP diagnosis by ultrasonography or histology up to 20-24 weeks of gestation1 (Box 1). European society of Human Reproduction and Embryology (ESHRE)/ American Society

for Reproductive Medicine (ASRM) guidelines consider recurrent pregnancy loss to be the failure of at least two clinically recognized pregnancies . However, especially important to mention, ectopic pregnancies and molar pregnancies are not considered as part of recurrent pregnancy loss (1, 2) . The exact upper limit of miscarriage is mainly due to the legal definition of viability and differs in countries (12–28 weeks). The availability or absence of early pregnancy units also defines whether a loss is clinically acknowledged and what management is advised to the patient (2).

Organic compounds which contain nitrogen and oxygen as heteroatoms function as a vital chemical category because their various structural forms together with their intricate spectroscopic characteristics satisfy both pharmaceutical and material science requirements according to [1,2]. According to studies [3 , 4] azomethine C=N and amide functional groups lead to improved electronic delocalization in conjugated systems, which results in changed molecular structures and altered optical properties. Structural optimization allows scientists to study molecular stability and reactivity through its ability to provide precise molecular equilibrium structures together with their associated electronic configurations based on the findings of [5,6]. The B3LYP hybrid functional from Density Functional Theory (DFT) functions as the most accurate theoretical method for optimizing the molecular structures of medium-sized organic compounds that contain heteroatoms and halogens according to the findings of references [7 , 8]. Scientists use infrared (IR) spectroscopy as a powerful research tool which helps them study molecular vibrations while detecting specific functional groups that include C=O bonds and C=N bonds and N–H bonds according to [9,10]. The combination of experimental IR spectra and DFT-calculated vibrational frequencies allows scientists to identify molecular modes and validate the results of their molecular structure optimization process [11,12]. Ultraviolet-visible UV-Vis spectroscopy shows important details of electronic transitions which occur in conjugated organic systems through their $\pi \rightarrow \pi^*$ and $n \rightarrow \pi^*$ transitions [13,14]. The B3LYP method of time-dependent DFT TD-DFT calculations shows high accuracy for both UV-Vis spectrum reproduction and electronic excitation process analysis of the studied materials [15,16]. Nuclear magnetic resonance (NMR) spectroscopy functions as a critical instrument for molecular structure determination by enabling scientists to study electronic environments that surround nuclei through their measurement of ^1H and ^13C chemical shifts [17,18]. NMR calculations based on DFT show excellent agreement with experimental results when using the GIAO method and researchers use NMR to identify spectral patterns in organic materials [19,20]. The introduction of halogen atoms, specifically chlorine and bromine, leads to changes in molecular structure and electron distribution and spectroscopic behavior because of inductive and resonance effects [21,22]. The research investigates how substituents affect structural properties and spectroscopic characteristics through a comparison of parent compounds with their halogenated derivatives [23,24]. The researchers study $C_{16}H_{13}N_3O$ together with its bromo and chloro derivatives to determine their ideal molecular configurations and their infrared spectroscopic properties and their ultraviolet-visible electronic transition patterns and their nuclear magnetic resonance chemical shift results. The research uses experimental spectroscopic data together with DFT/B3LYP calculations to achieve a complete understanding of how molecular structure determines properties and how halogen substitution affects molecular behavior.

2. Computational Methods: The study makes use of the Gaussian 16 (Revision C.01) program [20] for all quantum chemical calculations; it is a common program widely in use everywhere. The B3LYP functional [25,8] was used to conduct density functional theory calculations which evaluated geometric optimizations and vibrational frequency analyses and Mulliken charge assessments and orbital energy assessments and UV excited-state

simulations. The structural and electronic results were assessed using two basis sets which were STO-3G* and 3-21G [26,27]. The researchers constructed initial geometric structures which they pre-optimized before conducting complete optimization at B3LYP/STO-3G* and B3LYP/3-21G tiers. The frequency calculations showed no imaginary modes which allowed researchers to create harmonic IR data that they used to compare with experimental results [28]. The determination of atomic charges used Mulliken population analysis [29] while the calculation of HOMO and LUMO energies enabled assessments of electronic structure and stability [30]. The TD-DFT method evaluated UV–Vis absorption properties by measuring the ten lowest single transitions which they used to create experimental spectra [31,32]. The method proposed by [28,33] enables the assignment of scaled harmonic frequencies and IR intensities to particular vibrational modes. The software Multiwavelength and Gauss View [34] enabled researchers to visualize the molecular orbital electronic distributions and their surfaces. The presentation of all energies occurs in Hartree's or electron volts while the optimized geometries are shown in Angstroms and degrees. The application of thermal corrections required standard statistical thermodynamic procedures which operated at 298.15 K [6].

3. Experimental Details: Indole-3-carbohydrazide (1.0 g, 0.0057 mol) was dissolved in 10 mL of ethanol. The solution received the addition of 0.0057 mol of each substituted aldehyde which included 4-bromobenzaldehyde (1.05 g), 4-chlorobenzaldehyde (0.80 g), 4-hydroxybenzaldehyde (0.69 g), 4-nitrobenzaldehyde (0.755 g), 4-(dimethyl amino) benzaldehyde (0.84 g), benzaldehyde (0.604 g), salicylaldehyde (0.69 g), anisaldehyde (0.77 g), and 2,4-dimethoxybenzaldehyde (0.94 g). The researchers prepared aldehyde solutions by dissolving each compound in 10 mL of ethanol that contained several drops of glacial acetic acid (GAA) which they then added to the carbohydrazide solution while stirring until they achieved a clear homogeneous mixture. The resulting reaction mixture was stirred and heated at 80 °C for 6 hours. The solid product which formed through the process was collected by filtration and then it underwent a washing process with chilled distilled water before it was dried and finally it was recrystallized from 75% ethanol to produce the hydrazone derivatives in their pure form, show in the table (1).

Table (1): Some chemical and physical properties of the prepared compounds.

Molecular Formula (M.F.)	Aryl Group (-Ar)	Colour	(M.Wt.)	M.P. (°C)	Yield (%)
$C_{16}H_{13}N_3O$	Phenyl	Pale Yellow	263.30	188-190	80
$C_{16}H_{12}BrN_3O$	4-Bromophenyl	Off-White	342.20	202-204	75
$C_{16}H_{12}ClN_3O$	4-Chlorophenyl	White	297.75	198-200	82

4. Results and Discussion:

4.1. Molecular Geometry: From Fig (1) and table (2) show the study used DFT/B3LYP with STO-3G* and 3-21G basis sets to determine the optimized geometrical parameters of A1 ($C_{16}H_{13}N_3O$), A2 ($C_{16}H_{12}BrN_3O$), and A3 ($C_{16}H_{12}ClN_3O$) which demonstrated systematic basis-set effects that had valid chemical significance. The 3-21G results for A1 show that most C–C and C–N bond lengths are shorter than those from STO-3G* because the split-valence basis improves electron delocalization and polarization effects. The DFT studies demonstrate that minimal basis sets produce bond length overestimations because they fail to accurately describe electron density distribution through their restricted flexibility [7,8-35]. A1 displays small bond angle changes which remain consistent throughout its measurement range of 1–2° demonstrating the material's geometric relaxation behavior which occurs through larger basis set application. Conjugated nitrogen-containing systems have shown that extended basis sets produce realistic molecular geometries while they decrease artificial strain through their implementation of basic angle structure corrections

[36,37]. The 3-21G calculations of A1 show that dihedral angles tend to reach 0° or 180° which indicates that the molecule gains increased planarity and π-conjugation properties that match previous B3LYP studies about conjugated organic molecules [38,39]. The C–Br bond length in brominated derivative A2 shows an increase when calculated through 3-21G compared to STO-3G* which demonstrates how essential diffuse and polarization functions are for modeling heavy atomic elements. The results show that minimal basis sets consistently produce bond length measurements which fall short for bromine bonds while split-valence basis sets deliver values which better match actual experimental results [22–5,40]. The small changes in bond angle and dihedral angle which occur around the brominated carbon demonstrate that the overall molecular structure remains mostly intact as 3-21G fine-tunes the internal structure of the molecule. The basis-set impact on chlorinated compound A3 shows stronger effects because the C–Cl bond length measurement through 3-21G results in substantially longer distances. The bond length extension matches DFT/B3LYP measurements of chlorinated organic compounds which show that STO-3G* fails to accurately assess C–Cl bond lengths because of its insufficient chlorine diffuse electron cloud representation [9,41,19]. The 3-21G calculations show improved steric and electronic balance through their slight bond angle decreases and minor dihedral changes which previous theoretical studies have also confirmed [42]. The current findings match previous research results because they demonstrate that STO-3G* accurately describes molecular shapes while 3-21G provides better structural details for halogenated compounds. The study results demonstrate how basis set selection affects geometry prediction accuracy, which in turn determines the dependability of molecular property calculations that include electronic structure and spectroscopic behavior [7,43,20].

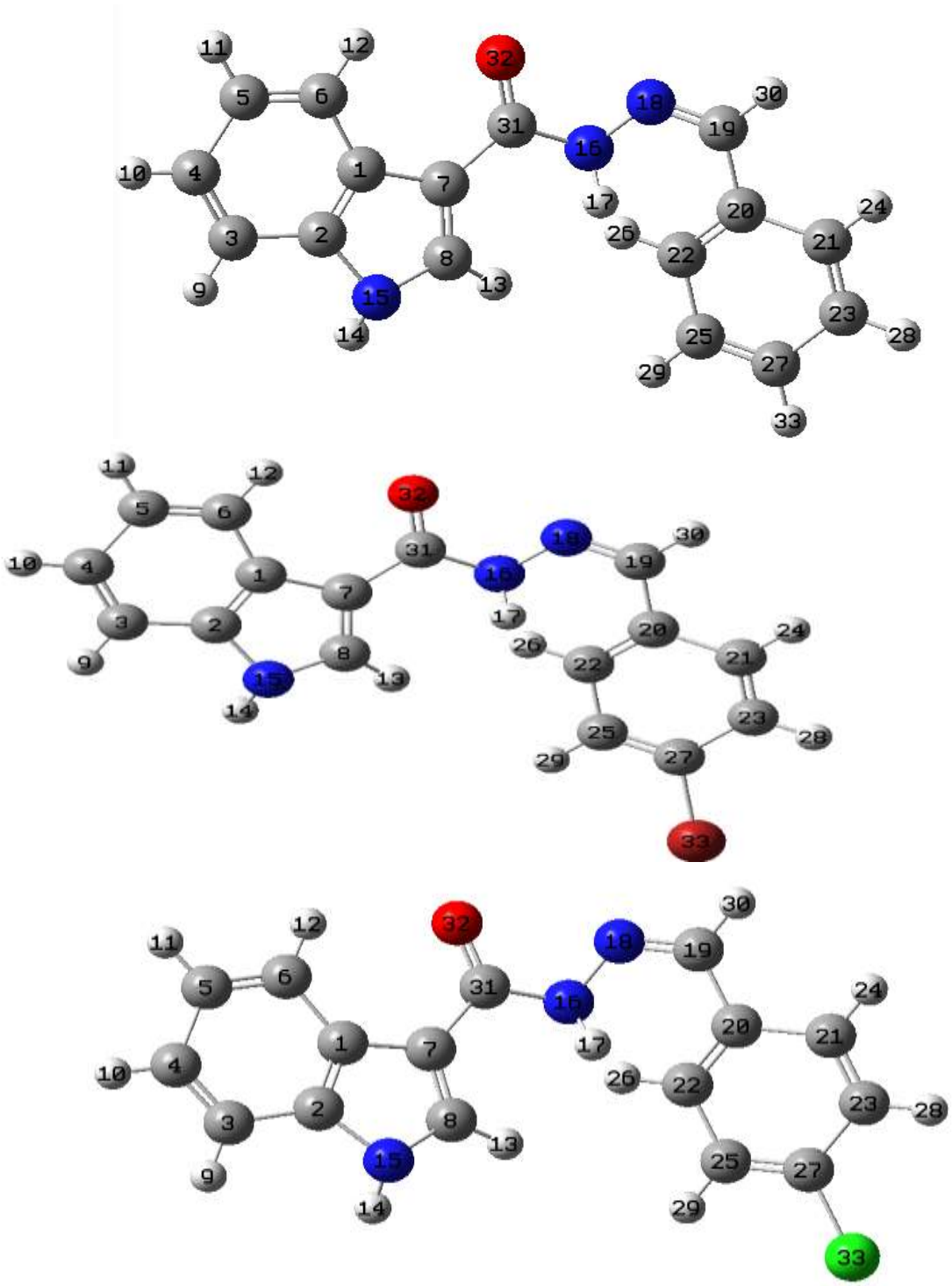

Fig (1): Optimized molecular geometries and atomic numbering of Compounds (A1,A2,and A3).

Table (2): Optimized geometric parameter of compound (A1,A2 and A3) using (DFT/B3LYP / STO-3G* and DFT/B3LYP /3-21G).

(A1) $C_{16}H_{13}N_3O$ DFT/B3LYP								
Bond length	**STO-3G***	**3-21G**	**Angle length**	**STO-3G***	**3-21G**	**Dihedral angle**	**STO-3G***	**3-21G**
R(1,2)	1.4339	1.4211	A(2,1,6)	118.9864	119.8125	D(6,1,2,3)	-0.0839	0.0117
R(1,6)	1.4213	1.403	A(2,1,7)	107.6588	107.201	D(6,1,2,15)	179.9755	179.9896
R(1,7)	1.4656	1.4488	A(6,1,7)	133.3547	132.9864	D(7,1,2,3)	179.8439	179.9706
R(2,3)	1.4168	1.3976	A(1,2,3)	122.5094	121.73	D(7,1,2,15)	-0.0966	-0.0516
R(2,15)	1.4192	1.393	A(1,2,15)	106.7335	107.0774	D(2,1,6,5)	0.029	-0.0227
R(3,4)	1.4002	1.3908	A(3,2,15)	130.7572	131.1925	D(2,1,6,12)	-179.6499	179.9946
R(3,9)	1.0974	1.0836	A(2,3,4)	117.0329	117.5503	D(7,1,6,5)	-179.8765	-179.969
R(4,5)	1.4256	1.4113	A(2,3,9)	121.3703	121.4992	D(7,1,6,12)	0.4446	0.0483
R(4,10)	1.0982	1.0838	A(4,3,9)	121.5968	120.9505	D(2,1,7,8)	0.2989	0.0586
R(5,6)	1.4	1.3892	A(3,4,5)	121.4328	121.2783	D(2,1,7,31)	179.4162	-179.9023
R(5,11)	1.0979	1.0837	A(3,4,10)	119.3716	119.3209	D(6,1,7,8)	-179.7879	-179.9902
R(6,12)	1.099	1.0802	A(5,4,10)	119.1956	119.4008	D(6,1,7,31)	-0.6706	0.0489
R(7,8)	1.3904	1.3823	A(4,5,6)	121.3657	121.2339	D(1,2,3,4)	0.0682	0.0004
R(7,31)	1.5158	1.4702	A(4,5,11)	118.932	119.1115	D(1,2,3,9)	-179.9902	180.0007
R(8,13)	1.0962	1.078	A(6,5,11)	119.7022	119.6546	D(15,2,3,4)	-180.007	-179.9714
R(8,15)	1.411	1.3861	A(1,6,5)	118.6727	118.395	D(15,2,3,9)	-0.0653	0.0288
R(14,15)	1.0423	1.0116	A(1,6,12)	119.6335	118.5465	D(1,2,15,8)	-0.1397	0.0259
R(16,17)	1.059	1.0189	A(5,6,12)	121.6929	123.0585	D(1,2,15,14)	-178.3109	179.8758
R(16,18)	1.4563	1.3955	A(1,7,8)	106.9647	106.8326	D(3,2,15,8)	179.9264	-179.9992
R(16,31)	1.4913	1.3992	A(1,7,31)	123.8293	122.8014	D(3,2,15,14)	1.7553	-0.1492
R(18,19)	1.3358	1.2955	A(8,7,31)	129.199	130.366	D(2,3,4,5)	0.0001	-0.0012
R(19,20)	1.5051	1.4809	A(7,8,13)	130.9392	130.4167	D(2,3,4,10)	179.9413	-179.9889
R(19,30)	1.1035	1.0864	A(7,8,15)	109.4685	109.3893	D(9,3,4,5)	-179.9414	-180.0014
R(20,21)	1.4226	1.4056	A(13,8,15)	119.583	120.1939	D(9,3,4,10)	-0.0002	0.0109
R(20,22)	1.4216	1.4086	A(2,15,8)	109.1731	109.4997	D(3,4,5,6)	-0.0532	-0.0105
R(21,23)	1.4052	1.3937	A(2,15,14)	125.6404	125.4663	D(3,4,5,11)	179.885	179.9947
R(21,24)	1.0988	1.0846	A(8,15,14)	125.1591	125.0338	D(10,4,5,6)	-179.9944	179.9772
R(22,25)	1.4077	1.3955	A(17,16,18)	114.3948	119.1804	D(10,4,5,11)	-0.0562	-0.0176
R(22,26)	1.0978	1.0841	A(17,16,31)	113.6762	120.806	D(4,5,6,1)	0.0371	0.0223
R(23,27)	1.4107	1.3978	A(18,16,31)	113.2648	119.0959	D(4,5,6,12)	179.7091	-179.9958

R(23,28)	1.0985	1.0838	A(16,18,19)	114.406	118.1995	D(11,5,6,1)	-179.9006	-179.983
R(25,27)	1.4087	1.3969	A(18,19,20)	131.5329	129.8175	D(11,5,6,12)	-0.2286	-0.0011
R(25,29)	1.0985	1.0841	A(18,19,30)	112.8908	114.2364	D(1,7,8,13)	178.4754	179.8352
R(27,33)	1.0983	1.0836	A(20,19,30)	115.5323	115.9431	D(1,7,8,15)	-0.3884	-0.0434
R(31,32)	1.2538	1.2372	A(19,20,21)	118.4636	119.0185	D(31,7,8,13)	-0.5784	-0.208
			A(19,20,22)	123.1517	122.2958	D(31,7,8,15)	-179.4422	179.9134
			A(21,20,22)	118.3378	118.6388	D(1,7,31,16)	172.5944	-179.8116
			A(20,21,23)	120.8738	120.7181	D(1,7,31,32)	-10.965	-0.5327
			A(20,21,24)	119.1766	119.1657	D(8,7,31,16)	-8.4951	0.2375
			A(23,21,24)	119.9488	120.1139	D(8,7,31,32)	167.9455	179.5164
			A(20,22,25)	120.5937	120.4778	D(7,8,15,2)	0.3376	0.0116
			A(20,22,26)	119.5577	119.5208	D(7,8,15,14)	178.5196	-179.8392
			A(25,22,26)	119.7976	119.944	D(13,8,15,2)	-178.6755	-179.8815
			A(21,23,27)	120.1246	120.1638	D(13,8,15,14)	-0.4934	0.2678
			A(21,23,28)	119.8588	119.84	D(17,16,18,19)	29.6633	10.8276
			A(27,23,28)	120.0161	119.9958	D(31,16,18,19)	162.113	179.9567
			A(22,25,27)	120.3643	120.275	D(17,16,31,7)	-32.4172	-5.4019
			A(22,25,29)	119.6758	119.7178	D(17,16,31,32)	151.0181	175.3168
			A(27,25,29)	119.9584	120.0003	D(18,16,31,7)	-165.2151	-174.3492
			A(23,27,25)	119.6856	119.705	D(18,16,31,32)	18.2202	6.3694
			A(23,27,33)	120.1396	120.1357	D(16,18,19,20)	-0.3007	3.3481
			A(25,27,33)	120.1711	120.1546	D(16,18,19,30)	-177.7341	-175.9865
			A(7,31,16)	112.4681	114.2095	D(18,19,20,21)	-145.9724	-141.2601
			A(7,31,32)	125.2376	123.044	D(18,19,20,22)	36.5623	41.2673
			A(16,31,32)	122.1956	122.7423	D(30,19,20,21)	31.4072	38.0651
						D(30,19,20,22)	-146.0581	-139.4074
						D(19,20,21,23)	-179.1478	-179.1969
						D(19,20,21,24)	1.1752	1.3632
						D(22,20,21,23)	-1.5587	-1.6311
						D(22,20,21,24)	178.7643	178.929
						D(19,20,22,25)	178.5346	178.7806
						D(19,20,22,26)	1.1371	1.5373
						D(21,20,22,25)	1.0662	1.2989
						D(21,20,22,26)	-176.3312	-175.9445
						D(20,21,23,27)	0.7865	0.7192

						D(20,21,23,28)	-179.4666	-179.4993
						D(24,21,23,27)	-179.539	-179.8462
						D(24,21,23,28)	0.2078	-0.0647
						D(20,22,25,27)	0.1961	-0.0564
						D(20,22,25,29)	-179.3647	-179.0945
						D(26,22,25,27)	177.5873	177.1752
						D(26,22,25,29)	-1.9735	-1.8628
						D(21,23,27,25)	0.5069	0.5522
						D(21,23,27,33)	179.8057	179.7648
						D(28,23,27,25)	-179.2395	-179.2291
						D(28,23,27,33)	0.0592	-0.0165
						D(22,25,27,23)	-0.9958	-0.8808
						D(22,25,27,33)	179.7056	179.9068
						D(29,25,27,23)	178.5637	178.1546
						D(29,25,27,33)	-0.7348	-1.0579
(A2) $C_{16}H_{12}BrN_3O$								
R(27,33)	1.8876	1.9282	A(23,27,33)	120.1171	119.8501	D(21,23,27,33)	-179.9695	179.994
			A(25,27,33)	120.0565	119.8028	D(28,23,27,33)	0.2255	0.1681
						D(22,25,27,33)	179.4077	179.673
						D(29,25,27,33)	-1.0732	-1.28
(A3) $C_{16}H_{12}ClN_3O$								
R(27,33)	1.758	1.8295	A(23,27,33)	119.7514	118.916	D(21,23,27,33)	-179.9444	-179.8805
			A(25,27,33)	119.7562	118.884	D(28,23,27,33)	0.2447	0.2537
						D(22,25,27,33)	179.422	179.5498
						D(29,25,27,33)	-1.0575	-1.4158

.

2. Mullikan Charge: In the table (3) show the DFT/B3LYP method with two basis sets, STO-3G* and 3-21G, was used to calculate Mulliken atomic charge distributions for A1 ($C_{16}H_{13}N_3O$), A2 ($C_{16}H_{12}BrN_3O$), and A3 ($C_{16}H_{12}ClN_3O$) to study how halogen substitution and different basis-set sizes affect charge distribution. The three substances show that when switching from STO-3G* to 3-21G, the total Mulliken charge values increase because 3-21G provides better measurements of polarization together with electron delocalization, which has been demonstrated in earlier DFT research [7,5]. The carbon framework shows that most aromatic carbon atoms (C3–C7, C21–C25) obtain more negative charges at the 3-21G level because their π-electron distribution across the conjugated system has improved. The positive charge of C2 increases from approximately +0.08 at STO-3G* to +0.37 at 3-21G in all three compounds, which shows that it is pulling electrons away from nearby heteroatoms more effectively. Charge redistribution patterns that occur in conjugated heteroaromatic systems with split-valence basis sets show similarity to previously documented results [6,22]. The hydrogen atoms (H9–H14, H24, H26, H28–H30) demonstrate higher positive charges at 3-21G because they increase C–H and N–H bond polarization. The behavior of the system shows consistency with earlier research which established that minimal basis sets produce lower estimates of hydrogen polarization while they also fail to capture bond dipoles with correct accuracy [19,5]. The basis-set dependence shows highest value for nitrogen atoms N15 N16 and N18. In A1, for example, N15 changes from about −0.27 (STO-3G*) to −0.81 (3-21G), with nearly identical values observed in A2 and A3. The negative charge increased because polarization effects enabled nitrogen atoms to better localize their lone-pair electrons while their electron-withdrawing power reached stronger levels. DFT studies that examine N-rich organic compounds establish these particular trends which scientists need to understand both hydrogen bonding processes and chemical reactions [8,12].The 3-21G level shows that O32 becomes much more negative with a value of approximately −0.49 which demonstrates that advanced basis sets provide more accurate representation of lone-pair density and anisotropic charge distribution around electronegative atoms. Oxygen charge magnitude increases in systems with carbonyl groups according to computational research results from [9,14].Halogen substitution significantly modifies the local charge distribution according to the comparison between A1 and A2 and A3 findings. The halogen atoms (Br33 and Cl33) in A2 and A3 show major charge alterations when they switch to the 3-21G basis while charge redistribution happens around the bonded carbon C27 point. The effect shows greater impact for bromine than chlorine which matches bromine's increased polarizability. Previous studies have established that heavier halogens need basis sets with more flexibility to achieve precise charge transfer and polarization effect measurements [13].

Table (3): The Mulliken charge distribution for the(A1) (C16H13N3O), (A2) (C16H12BrN3O) and(A3) (C16H12ClN3O) molecule using DFT/B3LYP (STO-3G* and 3-21G).

(A1) $C_{16}H_{13}N_3O$			**(A2) ($C_{16}H_{12}BrN_3O$)**			**(A3) ($C_{16}H_{12}ClN_3O$)**		
DFT/B3LYP			**DFT/B3LYP**			**DFT/B3LYP**		
Atoms	STO-3G*	3-21G	Atoms	STO-3G*	3-21G	Atoms	STO-3G*	3-21G
C1	-0.013674	0.010916	C1	-0.013476	0.011809	C1	-0.013461	0.012283
C2	0.076397	0.366025	C2	0.076713	0.36598	C2	0.076741	0.366065
C3	-0.09619	-0.190227	C3	-0.095734	-0.189821	C3	-0.095732	-0.18978
C4	-0.078583	-0.186659	C4	-0.078138	-0.186452	C4	-0.078117	-0.186382
C5	-0.085004	-0.188168	C5	-0.084546	-0.187849	C5	-0.084525	-0.187532
C6	-0.079586	-0.224721	C6	-0.079506	-0.224612	C6	-0.079509	-0.224702
C7	-0.05541	-0.111102	C7	-0.055686	-0.111861	C7	-0.055633	-0.112144
C8	0.002864	0.091044	C8	0.003345	0.092236	C8	0.003316	0.092799
H9	0.077447	0.176122	H9	0.078121	0.177169	H9	0.078151	0.177711
H10	0.077999	0.184181	H10	0.078624	0.185148	H10	0.078655	0.185648
H11	0.077945	0.185016	H11	0.078489	0.185859	H11	0.078513	0.186261
H12	0.095248	0.220163	H12	0.095299	0.220142	H12	0.095425	0.220064
H13	0.09139	0.20735	H13	0.091175	0.207024	H13	0.090913	0.207081
H14	0.230507	0.325164	H14	0.231491	0.326288	H14	0.231547	0.326831
N15	-0.267601	-0.812731	N15	-0.266999	-0.812335	N15	-0.266958	-0.812049
N16	-0.231493	-0.592101	N16	-0.230505	-0.59107	N16	-0.23065	-0.590456
H17	0.188954	0.331635	H17	0.188868	0.330146	H17	0.188781	0.329927
N18	-0.122969	-0.239583	N18	-0.119949	-0.238651	N18	-0.119831	-0.236321
C19	-0.012847	0.064343	C19	-0.013028	0.066137	C19	-0.012831	0.065744
C20	-0.016326	-0.065301	C20	-0.012827	-0.067355	C20	-0.013497	-0.067868
C21	-0.074115	-0.179703	C21	-0.070473	-0.174413	C21	-0.069394	-0.17084
C22	-0.086977	-0.223458	C22	-0.083327	-0.216434	C22	-0.082198	-0.211759
C23	-0.077597	-0.179914	C23	-0.069834	-0.14272	C23	-0.072825	-0.151066
H24	0.082865	0.197155	H24	0.08914	0.20498	H24	0.089874	0.208776
C25	-0.079615	-0.18278	C25	-0.07178	-0.144949	C25	-0.074937	-0.153653
H26	0.088398	0.204985	H26	0.094742	0.212526	H26	0.095674	0.216438
C27	-0.076593	-0.184176	C27	0.005669	-0.339924	C27	0.096167	-0.266693
H28	0.083244	0.196341	H28	0.096269	0.215609	H28	0.099231	0.225519
H29	0.080586	0.19353	H29	0.093648	0.213117	H29	0.096604	0.223297
H30	0.090376	0.221203	H30	0.092192	0.223065	H30	0.092278	0.224485
C31	0.213465	0.680602	C31	0.214256	0.679771	C31	0.214262	0.679265
O32	-0.185449	-0.489765	O32	-0.183202	-0.487669	O32	-0.183321	-0.486685
H33	0.082345	0.194615	Br33	-0.079029	0.199111	Cl33	-0.172714	0.099738

3.Vibrational Spectral Analysis

3.1. $C_{16}H_{13}N_3O$: Table (4) show the infrared (IR) vibrational frequencies of the indole-based compound $C_{16}H_{13}N_3O$ were determined through Density Functional Theory (DFT) calculations at the B3LYP level using the STO-3G* and 3-21G basis sets. The researchers used the calculated frequencies to establish reliable vibrational mode assignments through comparison with experimental IR data which also helped them validate the optimized molecular structure. The N–H stretching vibrations of the indole and amide moieties create the high-frequency region which extends from 3450 to 3320 cm^{-1}. The experimental band observed at 3211 cm^{-1} appears at a lower wavenumber compared to the calculated values which can be ascribed to hydrogen bonding and intermolecular interactions present in the

solid phase effects that are not fully captured in gas-phase DFT calculations. The aromatic C–H stretching vibrations were calculated in the range 3100–3020 cm^{-1} which showed good agreement with the experimental band at 3061 cm^{-1}. The aliphatic C–H stretching modes were predicted in the region 2960–2870 cm^{-1} which confirmed the presence of alkyl fragments within the molecular framework. The amide I ν(C=O) stretching vibration produces a strong band which extends from 1685 to 1650 cm^{-1}. The experimental mode shows a slight red shift at 1632 cm^{-1} because of conjugation effects and intermolecular interactions. The bands observed in the range 1595–1530 cm^{-1} are assigned to ν(C=N) stretching coupled with amide II vibrations, with the experimental counterpart located at 1547 cm^{-1}, confirming the existence of the azomethine linkage. The stretching vibrations of aromatic ring compounds at 1510–1460 cm^{-1} match with the experimental measurement which occurs at 1493 cm^{-1}. The additional bands which emerge at 1462 and 1376 cm^{-1} result from in-plane δ(C–H) bending and C–C skeletal vibrations of the aromatic rings. The C–N stretching modes were identified in the range 1380–1320 cm^{-1} with an experimental peak observed at 1315 cm^{-1} which provided evidence for the existence of amide and heteroatomic linkages. The region 1290–1120 cm^{-1} contains vibrational modes which were linked to dual ν(C–N) and ν(C–O) stretching movements together with aromatic in-plane ring vibrations. The experimental bands at 1245 and 1199 cm^{-1} further corroborate these assignments. The bands located between 1100 and 1000 cm^{-1} correspond to in-plane δ(C–H) bending vibrations of the aromatic system. The experimental results showed out-of-plane aromatic C–H bending vibrations which are specific to substituted benzene and indole rings at 894, 838, and 772 cm^{-1} and the theoretical calculations produced accurate results. The low-frequency region (650–400 cm^{-1}) is associated with skeletal ring deformation and lattice vibrations which arise from collective molecular motions [44,45].

3.2. $C_{16}H_{12}BrN_3O$: Table (5) show the FT-IR vibrational frequencies of compound $C_{16}H_{12}BrN_3O$ were analyzed experimentally and theoretically using the DFT/B3LYP method with STO-3G* and 3-21G basis sets. The experimental and theoretical results of the study achieved good agreement with each other which validated the optimized molecular structure through their comparison of calculated and measured frequencies.The N–H stretching vibration is observed experimentally at 3121 cm^{-1} which corresponds well with the calculated ranges 3440–3360 cm^{-1} STO-3G* and 3460–3360 cm^{-1} 3-21G. The calculated values exhibit slight overestimation because DFT calculations usually apply harmonic approximation as their standard method. The aromatic C–H stretching vibrations appear experimentally at 3017 cm^{-1} while the calculated frequencies exist between 3110–3030 cm^{-1} STO-3G* and 3105–3035 cm^{-1} 3-21G. The molecular structure contains aromatic rings because this finding establishes their existence. The aliphatic C–H stretching modes are experimentally observed at 2943 and 2895 cm^{-1} which matches the calculated ranges of 2960–2870 cm^{-1} STO-3G* and 2965–2880 cm^{-1} 3-21G. The experimental band at 1705 cm^{-1} originates from amide C=O stretching which produces the amide I vibration. The theoretical values show excellent consistency with measurement results because they range from 1700 to 1660 cm^{-1} for STO-3G* and 1690 to 1660 cm^{-1} for 3-21G. The experimental band at 1778 cm^{-1} represents carbonyl stretching which the conjugation effects caused to occur at higher frequencies. The C=N stretching vibration is experimentally detected at 1623 cm^{-1} while the calculated values occur at 1615–1580 cm^{-1} (STO-3G*) and 1605–1540 cm^{-1} (3-21G) .The stretching vibrations of aromatic C=C bonds have been experimentally detected at two specific wavelengths, 1595 cm^{-1} and 1539 cm^{-1}, which match the theoretical predictions for two frequency ranges, 1580–1520 cm^{-1} and 1515–1465 cm^{-1}. The region between 1487 and 1449 cm^{-1} contains bands which scientists associate with aromatic C–H bending vibrations because they match the theoretical predictions which show ranges between 1450 and 1410 cm^{-1} for both basis sets. The C–N stretching vibrations appear experimentally at 1345 and 1317 cm^{-1}, in agreement with the

theoretical ranges 1380–1320 cm^{-1} (STO-3G*) and 1385–1325 cm^4 (3-21G). The mixed C–N and C–O stretching vibrations are observed experimentally at 1272 and 1228 cm^{-1}, matching the calculated region 1290–1240 cm^{-1}. The experimental identification of aromatic in-plane ring vibrations occurs at 1193 cm^{-1}, while the theoretical values exist within the 1200–1130 cm^{-1} range. The experimental observation of in-plane C–H bending vibrations occurs at 1070 cm^{-1}, which matches the calculated range of 1100–1020 cm^{-1}. The ring deformation modes which scientists observed at 922 cm^{-1} show support from calculated frequencies which fall within the 980–920 cm^{-1} frequency range. The out-of-plane aromatic C–H bending vibrations are clearly observed experimentally at 892, 840, 814, 773, and 747 cm^{-1}, which correspond well to the calculated regions 900–820 cm^{-1} and 800–730 cm^{-1}, confirming the substituted aromatic system. The presence of bromine in the molecule is confirmed by the C–Br stretching vibrations, which scientists observed experimentally at 658 and 583 and 515 cm^{-1}, and these results match perfectly with the calculated ranges 660–520 cm^{-1} (STO-3G*) and 670–560 cm^{-1} (3-21G). The lower frequency bands which appear below 520 cm^{-1} stem from both skeletal vibrations and lattice vibrations[44,45]., as shown in the table(4).

3.3.$C_{16}H_{12}ClN_3O$: In table (6) show the FT-IR vibrational spectra of compound $C_{16}H_{12}ClN_3O$ were investigated experimentally and theoretically using the DFT/B3LYP method with STO-3G* and 3-21G basis sets to confirm molecular structure and identify specific vibrational modes. The calculated frequencies match the experimental results, which confirms that the optimized molecular geometry is correct. The N–H stretching vibration, which is found in the indole/amide group, has an experimental measurement of 3127 cm^{-1}. The corresponding calculated frequencies appear in the ranges 3445–3350 cm^{-1} for STO-3G* and 3460–3360 cm^{-1} for 3-21G. The upward shift in theoretical values occurs because the gas-phase calculations use harmonic approximation and lack intermolecular interactions. The experimental detection of aromatic C–H stretching vibrations occurs at 3065 cm^{-1} while the calculated values lie in the regions 3110–3040 cm^{-1} for STO-3G* and 3105–3035 cm^{-1} for 3-21G. The bands demonstrate that the molecular structure contains aromatic ring systems for their identification. The aliphatic C–H stretching modes are detected at 2943 and 2895 cm^{-1} which match the calculated ranges of 2960–2880 cm^{-1} for STO-3G* and 2965–2880 cm^{-1} for 3-21G. The amide C=O stretching vibration, which produces an experimental absorption band at 1624 cm^{-1}, is designated as amide I. The mode has theoretical predictions at 1695–1665 cm^{-1} for STO-3G* and at 1690–1660 cm^{-1} for 3-21G which exhibit good agreement with the experimental results. DFT calculations show a standard frequency deviation which researchers can fix through their use of proper scaling methods. Scientists detect the C=N stretching vibration which occurs in azomethine groups at a wavelength of 1600 cm^{-1}. The theoretical bands of the study appear within the following spectral ranges 1610–1550 cm^{-1} for STO-3G* and 1605–1540 cm^{-1} for 3-21G. The experimental results show that the aromatic C=C stretching vibrations occur at 1539 and 1492 cm^{-1} which match the calculated ranges of 1515–1470 cm^{-1} and 1515–1465 cm^{-1}. The experimental spectrum shows two bands at 1449 cm^{-1} and 1375 cm^{-1} which scientists identify as aromatic C–H bending vibrations. The two modes of the study match the calculated regions which span 1460–1420 cm^{-1} and 1455–1415 cm^{-1} for both basis sets. Scientists measure the C–N stretching vibrations at 1318 cm^{-1} while theoretical predictions show an expected range of 1385–1330 cm^{-1} for STO-3G* and 1385–1325 cm^{-1} for 3-21G. The experimental measurement of mixed C–N and C–O stretching vibrations shows a result of 1277 cm^{-1} which falls within the expected range of 1295–1245 cm^{-1} for both basis sets. The aromatic in-plane ring vibrations appear experimentally at 1192 cm^{-1}, while the corresponding calculated modes fall in the 1210–1135 cm^{-1} (STO-3G*) and 1210–1130 cm^{-1} (3-21G) regions.The in-plane C–H bending vibrations are experimentally detected at 1087 and 1013 cm^{-1}, which correspond well with the calculated ranges 1105–1030 cm^{-1} and 1105–

1025 cm^{-1}. The ring deformation modes observed at 923 cm^{-1} are supported by theoretical values in the 1000–930 cm^{-1} and 995–925 cm^{-1} regions.The out-of-plane aromatic C–H bending vibrations, characteristic of substituted aromatic systems, are experimentally observed at 893, 841, 819, 774, and 747 cm^{-1}. The experimental bands of the substituted benzene/indole structure show perfect match with the calculated regions 910–830 cm^{-1} and 800–720 cm^{-1}. The chlorine presence in the molecule has been clearly established through the C–Cl stretching vibrations, which show experimental results at 645, 585, and 515 cm^{-1}. Theoretical predictions state that these modes will occur in the 680–560 cm^{-1} region, which applies to both STO-3G* and 3-21G basis sets. Skeletal and lattice vibrations[44,45] account for all remaining low-frequency bands that exist below 500 cm^{-1}.

Table (4): Comparison of Experimental and DFT/B3LYP (STO-3G and 3-21G) Infrared Vibrational Frequencies of ($C_{16}H_{13}N_3O$) Compound.

Wavenumber (cm^{-1})		Functional group assignment		Wavenumber (cm^{-1})	Functional group assignment
DFT/B3LYP STO-3G*	DFT/B3LYP 3-21G	DFT/B3LYP/STO-3G*	DFT/B3LYP/3-21G	Experimental	
3440–3320	3450–3350	ν(N–H) stretching (indole / amide)	ν(N–H) stretching (indole / amide)	3211	ν(N–H) stretching (indole / amide)
3100–3020	3100–3030	ν(C–H) aromatic stretching	ν(C–H) aromatic stretching	3061	ν(C–H) aromatic stretching
2950–2850	2960–2870	ν(C–H) aliphatic stretching	ν(C–H) aliphatic stretching		
1690–1650	1685–1650	ν(C=O) amide I stretching	ν(C=O) amide I stretching	1632	ν(C=O) amide I stretching
1585–1520	1595–1530	ν(C=N) stretching / amide II	ν(C=N) stretching / amide II	1547	ν(C=N) stretching / amide II
1500–1450	1510–1460	ν(C=C) aromatic ring stretching	ν(C=C) aromatic ring stretching	1493	ν(C=C) aromatic ring stretching
1440–1400	1450–1410	δ(C–H) aromatic bending	δ(C–H) aromatic bending	1462	δ(C–H) aromatic bending
				1433	ν(C–C) aromatic stretching
				1376	δ(C–H) in-plane bending
1370–1320	1380–1320	ν(C–N) stretching	ν(C–N) stretching	1315	ν(C–N) stretching
				1245	ν(C–N) amide stretching
1280–1230	1290–1240	ν(C–N) / ν(C–O) stretching	ν(C–N) / ν(C–O) stretching	1199	ν(C–N) / ν(C–O) stretching
1200–1100	1200–1120	in-plane aromatic ring vibrations	aromatic in-plane ring vibrations	1110	ν(C–N) stretching
				1093	ν(C–O) / ring vibration
				1073	ν(C–C) aromatic stretching
1080–1000	1100–1020	δ(C–H) in-plane bending	δ(C–H) in-plane bending	1010	δ(C–H) in-plane bending
980–900	990–920	ring deformation modes	ring deformation modes	983	ring deformation vibration
890–820	900–820	γ(C–H) aromatic out-of-plane	γ(C–H) aromatic out-of-plane bending	894	γ(C–H) out-of-plane bending
				838	γ(C–H) aromatic bending
780–700	790–700	γ(C–H) out-of-plane (substituted benzene)	γ(C–H) out-of-plane (substituted benzene / indole)	772	γ(C–H) out-of-plane (substituted benzene)
				749	γ(C–H) aromatic bending
				694	γ(C–H) aromatic bending
650–550	670–550	skeletal ring deformation	skeletal ring deformation	638	ring deformation
				608	skeletal vibration
				558	ring deformation
				503	skeletal vibration

				478	skeletal vibration
540–400	540–420	lattice / skeletal vibrations	lattice / skeletal vibrations	432	lattice / skeletal vibration
				421	lattice / skeletal vibration

Table (5): Comparison of Experimental and DFT/B3LYP (STO-3G and 3-21G) Infrared Vibrational Frequencies of ($C_{16}H_{12}BrN_3O$) Compound.

Wavenumber (cm^{-1})		Functional group assignment		Wavenumber (cm^{-1})	Functional group assignment
DFT/B3LYP STO-3G*	DFT/B3LYP 3-21G	DFT/B3LYP/STO-3G*	DFT/B3LYP/3-21G	Experimental	
3440–3360	3460–3360	ν(N–H) stretching (indole / amide)	ν(N–H) stretching (indole / amide)	3121	ν(N–H) stretching (indole / amide)
3110–3030	3105–3035	ν(C–H) aromatic stretching	ν(C–H) aromatic stretching	3017	ν(C–H) aromatic stretching
2960–2870	2965–2880	ν(C–H) aliphatic stretching	ν(C–H) aliphatic stretching	2943	ν(C–H) aliphatic stretching
				2895	ν(C–H) aliphatic stretching
				1778	ν(C=O) stretching (carbonyl)
1700–1660	1690–1660	ν(C=O) amide I stretching	ν(C=O) amide I stretching	1705	ν(C=O) amide I stretching
1615–1580	1605–1540	ν(C=N) stretching	ν(C=N) stretching / amide II	1623	ν(C=N) stretching
1580–1520	1515–1465	ν(C=C) aromatic stretching		1595	ν(C=C) aromatic stretching
1500–1460		ν(C=C) aromatic / δ(C–H) bending	ν(C=C) aromatic ring stretching	1539	ν(C=C) aromatic stretching
1450–1410	1455–1415	δ(C–H) aromatic bending	δ(C–H) aromatic bending	1487	δ(C–H) aromatic bending
				1449	δ(C–H) aromatic bending
				1375	δ(C–H) bending
1380–1320	1385–1325	ν(C–N) stretching	ν(C–N) stretching	1345	ν(C–N) stretching
				1317	ν(C–N) stretching
1290–1240	1295–1245	ν(C–N) / ν(C–O) stretching	ν(C–N) + ν(C–O) stretching	1272	ν(C–N) / ν(C–O) stretching
				1228	ν(C–O) stretching
1200–1130	1210–1130	aromatic in-plane ring vibrations	aromatic in-plane ring vibrations	1193	aromatic ring vibration
				1151	ν(C–N) stretching
				1122	ν(C–N) stretching
1100–1020	1105–1025	δ(C–H) in-plane bending	δ(C–H) in-plane bending	1070	δ(C–H) in-plane bending
980–920	995–925	ring deformation modes	ring deformation modes	922	ring deformation
				892	γ(C–H) out-of-plane bending
900–820	905–825	γ(C–H) aromatic out-of-plane bending	γ(C–H) aromatic out-of-plane bending	840	γ(C–H) aromatic out-of-plane
				814	γ(C–H) aromatic bending
800–730	795–710	γ(C–H) out-of-plane (substituted benzene / indole)	γ(C–H) out-of-plane (substituted benzene / indole)	773	γ(C–H) out-of-plane (substituted benzene)
				747	γ(C–H) out-of-plane bending

690–620		skeletal ring deformation		706	aromatic ring deformation
660–520	670–560	ν(C–Br) stretching	ν(C–Br) stretching vibration	658	ν(C–Br) stretching
				583	ν(C–Br) stretching
				515	ν(C–Br) / skeletal vibration
				475	skeletal vibration
520–420	545–430	skeletal / lattice vibrations	skeletal / lattice vibrations	421	lattice / skeletal vibration

Table (6): Comparison of Experimental and DFT/B3LYP (STO-3G and 3-21G) Infrared Vibrational Frequencies of ($C_{16}H_{12}ClN_3O$) Compound.

Wavenumber (cm^{-1})		Functional group assignment		Wavenumber (cm^{-1})	Functional group assignment
DFT/B3LYP STO-3G*	DFT/B3LYP 3-21G	DFT/B3LYP/STO-3G*	DFT/B3LYP/3-21G	Experimental	
3445–3350	3460–3360	ν(N–H) stretching (indole / amide)	ν(N–H) stretching (indole / amide)	3127	ν(N–H) stretching (indole / amide)
3110–3040	3105–3035	ν(C–H) aromatic stretching	ν(C–H) aromatic stretching	3065	ν(C–H) aromatic stretching
2960–2880	2965–2880	ν(C–H) aliphatic stretching	ν(C–H) aliphatic stretching	2943	ν(C–H) aliphatic stretching
				2895	ν(C–H) aliphatic stretching
1695–1665	1690–1660	ν(C=O) amide I stretching	ν(C=O) amide I stretching	1624	ν(C=O) amide I stretching
1610–1550	1605–1540	ν(C=N) stretching / amide II	ν(C=N) stretching / amide II	1600	ν(C=N) stretching
1515–1470	1515–1465	ν(C=C) aromatic ring stretching	ν(C=C) aromatic ring stretching	1539	ν(C=C) aromatic stretching
				1492	ν(C=C) aromatic stretching
1460–1420	1455–1415	δ(C–H) aromatic bending	δ(C–H) aromatic bending	1449	δ(C–H) aromatic bending
				1375	δ(C–H) bending
1385–1330	1385–1325	ν(C–N) stretching	ν(C–N) stretching	1318	ν(C–N) stretching
1295–1245	1295–1245	ν(C–N) + ν(C–O) stretching	ν(C–N) + ν(C–O) stretching	1277	ν(C–N) / ν(C–O) stretching
1210–1135	1210–1130	aromatic in-plane ring vibrations	aromatic in-plane ring vibrations	1192	aromatic ring vibration
				1152	ν(C–N) stretching
				1123	ν(C–N) stretching
1105–1030	1105–1025	δ(C–H) in-plane bending	δ(C–H) in-plane bending	1087	δ(C–H) in-plane bending
				1013	δ(C–H) in-plane bending
1000–930	995–925	ring deformation modes	ring deformation modes	923	ring deformation
910–830	905–825	γ(C–H) aromatic out-of-plane bending	γ(C–H) aromatic out-of-plane bending	893	γ(C–H) aromatic out-of-plane
				841	γ(C–H) aromatic out-of-plane
				819	γ(C–H) aromatic bending
800–720	795–710	γ(C–H) out-of-plane (substituted benzene / indole)	γ(C–H) out-of-plane (substituted benzene / indole)	774	γ(C–H) out-of-plane (substituted benzene)
				747	γ(C–H) out-of-plane bending
				645	ν(C–Cl) stretching
				585	ν(C–Cl) stretching

680–560	680–560	ν(C–Cl) stretching vibration	ν(C–Cl) stretching vibration	515	ν(C–Cl) / skeletal vibration
				475	skeletal vibration
545–430	545–430	skeletal / lattice vibrations	skeletal / lattice vibrations	419	lattice / skeletal vibration

4. UV–Vis Spectral Analysis: The study of electronic absorption spectra for compounds A1 through A3 used DFT/B3LYP with the STO-3G* and 3-21G basis sets to conduct both experimental and theoretical research according show table (7). The researchers evaluated how molecular structure and halogen substitution affected electronic transitions by comparing the computed maximum absorption wavelengths (λ_max) with the observed UV–Vis results. The experimental absorption maximum for compound A1 ($C_{16}H_{13}N_3O$) occurs at 282 nm, which closely matches the calculated values of 274.46 nm (STO-3G*) and 279.91 nm (3-21G). The experimental spectrum shows a small red shift when compared to the theoretical predictions because solvent effects and intermolecular interactions require gas-phase DFT calculations to handle them. The conjugated indole–imine system enables $\pi\rightarrow\pi^*$ transitions to happen which leads to the creation of an absorption band in this specific area. The experimental λ_max value of Compound A2 ($C_1{\cdot}H_{12}BrN_3O$) measures 285 nm while theoretical calculations predict 298.01 nm for STO-3G* and 288.35 nm for 3-21G. The introduction of the bromine atom causes a noticeable red shift in the absorption maximum compared to A1, which can be attributed to the heavy atom effect and increased conjugation, leading to a reduction in the HOMO–LUMO energy gap. The 3-21G basis set produced calculated values that matched experimental results more closely than other methods because it provided superior electronic structure details for halogenated compounds. The experimental absorption maximum for compound A3 ($C_{16}H_{12}ClN_3O$) occurs at 287 nm while theoretical values predict 295 nm (STO-3G*) and 304 nm (3-21G) respectively. Chlorine substitution affects electronic transitions according to the observed red shift which occurs when comparing A1 to other samples. The absorption band primarily results from $\pi\rightarrow\pi^*$ transitions which acquire partial $n\rightarrow\pi^*$ character because heteroatoms (N and O) exist in the molecular structure. The theoretical UV–Vis results match experimental data for all studied compounds at a reasonable level of agreement. Theoretical calculations show small discrepancies between calculated and experimental λ_max values which occur due to solvent effects and basis set limitations and the neglect of vibrational and environmental contributions, The idea of interpretation was also taken from the references[46,47]. The absorption maxima trend shows halogen substitution affects molecular electronic properties because A1 displays lower absorption maxima than both A2 and A3[48].

.

Table (7) : UV-Vis spectra between theoretical (DFT/B3LYP)(basis set /STO-3G* and 3-21G and experimental of compunds

Comp No.	Formula	Structure	(λ_{max})UV-Vis absorption spectrum (nm)(Theo)(DFT/B3LYP)		UV-Vis absorption spectrum (nm)(Expt)
			STO-3G*	3-21G	
A1	$C_{16}H_{13}N_3O$		274.46	279.91	282
A2	$C_{16}H_{12}BrN_3O$	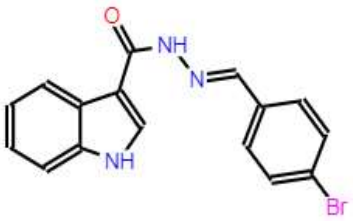	298.01	288.35	285
A3	$C_{16}H_{12}ClN_3O$	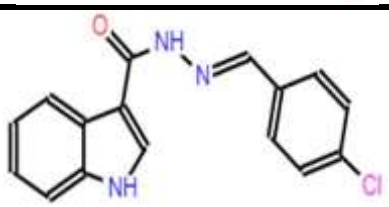	295	304	287

(A1,A2,and A3).

5. Conculsion

The researchers synthesized indole-based hydrazone derivatives A1, A2 and A3 with successful results which included high yield production and distinct melting point determination. The researchers studied the structural and spectroscopic characteristics of the substances through experimental methods and theoretical modeling. The researchers used the B3LYP functional together with STO-3G* and 3-21G basis sets to perform density functional theory calculations. Stable minimum-energy conformations with no imaginary frequencies were represented by the optimised molecular structures.The findings showed that the observed changes in the geometric measurements were directly influenced by the chosen basis set. When compared to STO-3G*, the 3-21G basis set produced bond lengths and bond angles with better accuracy. The results showed better outcomes for bonds which contained heteroatoms and halogen groups. The structural changes of halogenated derivatives showed the same polarizability behavior which bromine and chlorine atoms exhibited. The Mulliken charge analysis showed that nitrogen and oxygen atoms demonstrated strong capability to localize charge distribution. Bromine substitution led to greater electronic polarization in the molecular structure than chlorine substitution did. The vibrational frequency calculations matched the experimental FT-IR spectra with high accuracy. Theoretical results enabled the successful assignment of characteristic functional group vibrations. Researchers identified solid-state effects as the reason for minor frequency differences between experimental data and calculated results. The experimental findings received strong support from the computational results which provided robust evidence of their validity. The DFT/B3LYP methodology proves itself to be a dependable method for analyzing this type of system according to the study results. The researchers

established a solid basis which enables future research in chemical and pharmaceutical studies of indole-based hydrazone derivatives.

REFERENCES

[1] McMurry, J. (2016). Organic chemistry (9th ed.). Cengage Learning.

[2] Atkins, P., & de Paula, J. (2014). Physical chemistry (10th ed.). Oxford University Press.

[3] Katritzky, A. R., & Rees, C. W. (2008). Comprehensive heterocyclic chemistry. Elsevier.

[4] Lobana, T. S., et al. (2015). Structural and spectroscopic studies of heterocyclic compounds. Journal of Molecular Structure, 1097, 101–110. https://doi.org/10.1016/j.molstruc.2015.05.018

[5] Jensen, F. (2017). Introduction to computational chemistry (3rd ed.). Wiley.

[6] Cramer, C. J. (2013). Essentials of computational chemistry: Theories and models (2nd ed.). Wiley.

[7] Becke, A. D. (1993). Density-functional thermochemistry. III. The role of exact exchange. Journal of Chemical Physics, 98(7), 5648–5652. https://doi.org/10.1063/1.464913

[8] Lee, C., Yang, W., & Parr, R. G. (1988). Development of the Colle–Salvetti correlation-energy formula into a functional of the electron density. Physical Review B, 37(2), 785–789. https://doi.org/10.1103/PhysRevB.37.785

[9] Socrates, G. (2004). Infrared and Raman characteristic group frequencies: Tables and charts (3rd ed.). Wiley.

[10] Bellamy, L. J. (1980). The infrared spectra of complex molecules (2nd ed.). Springer.

[11] Sundaraganesan, N., et al. (2007). Vibrational spectroscopic and quantum chemical studies of organic molecules. Spectrochimica Acta Part A: Molecular and Biomolecular Spectroscopy, 67(3–4), 628–635. https://doi.org/10.1016/j.saa.2006.08.018

[12] Govindarajan, M., et al. (2017). Spectroscopic and DFT investigation of conjugated organic systems. Journal of Molecular Structure, 1137, 373–384. https://doi.org/10.1016/j.molstruc.2017.02.050

[13] Reichardt, C., & Welton, T. (2011). Solvents and solvent effects in organic chemistry (4th ed.). Wiley-VCH.

[14] Alparone, A. (2016). DFT and vibrational analysis of nitrogen-containing organic molecules. Spectrochimica Acta Part A: Molecular and Biomolecular Spectroscopy, 152, 30–37. https://doi.org/10.1016/j.saa.2015.07.047

[15] Casida, M. E. (2009). Time-dependent density functional response theory for molecules. Journal of Molecular Structure: THEOCHEM, 914, 3–18. https://doi.org/10.1016/j.theochem.2009.08.018

[16] Bauernschmitt, R., & Ahlrichs, R. (1996). Treatment of electronic excitations within the adiabatic approximation of time dependent density functional theory. Chemical Physics Letters, 256(4–5), 454–464. https://doi.org/10.1016/0009-2614(96)00440-X

[17] Keeler, J. (2010). Understanding NMR spectroscopy (2nd ed.). Wiley.

[18] Breitmaier, E. (2002). Structure elucidation by NMR in organic chemistry. Wiley.

[19] Ditchfield, R. (1974). Molecular orbital theory of magnetic shielding and magnetic susceptibility. Molecular Physics, 27(4), 789–807. https://doi.org/10.1080/00268977400100711

[20] Frisch, M. J., et al. (2016). Gaussian 16 (Revision A.03). Gaussian Inc.

[21] Hansch, C., Leo, A., & Hoekman, D. (1991). Exploring QSAR: Hydrophobic, electronic, and steric constants. Chemical Reviews, 91(2), 165–195. https://doi.org/10.1021/cr00002a004

[22] Politzer, S., et al. (2017). Analysis of molecular electrostatic potentials. Journal of Molecular Modeling, 23, 18. https://doi.org/10.1007/s00894-016-3185-0

[23] Arshad, M., et al. (2020). Structural and electronic properties of organic molecules: A DFT study. Journal of Molecular Structure, 1203, 127406. https://doi.org/10.1016/j.molstruc.2019.127406

[24] Mahmudov, A. R., et al. (2014). Noncovalent interactions in crystal engineering. CrystEngComm, 16, 7583–7593. https://doi.org/10.1039/C4CE00576A

[25] Raghavachari, K. (2000). Perspective on "Density functional thermochemistry. III. The role of exact exchange" Becke AD (1993) J Chem Phys 98: 5648–52. Theoretical Chemistry Accounts, 103(3), 361–363.

[26] Hehre, W. J., Ditchfield, R., & Pople, J. A. (1972). Self—consistent molecular orbital methods. XII. Further extensions of Gaussian—type basis sets for use in molecular orbital studies of organic molecules. The Journal of Chemical Physics, 56(5), 2257–2261.

[27] Binkley, J. S., Pople, J. A., & Hehre, W. J. (1980). Self-consistent molecular orbital methods. 21. Small split-valence basis sets for first-row elements. Journal of the American Chemical Society, 102(3), 939–947.

[28] Scott, A. P., & Radom, L. (1996). Harmonic vibrational frequencies: An evaluation of Hartree-Fock, Moller-Plesset, quadratic configuration interaction, density functional theory, and semiempirical scale factors. Journal of Physical Chemistry, 100, 16502–16513.

[29] Mulliken, R. S. (1955). Electronic population analysis on LCAO–MO molecular wave functions. I. The Journal of Chemical Physics, 23(10), 1833–1840.

[30] Parr, R. G., & Yang, W. (1989). Density Functional Theory of Atoms and Molecules. Oxford University Press, Oxford.

[31] Runge, E., & Gross, E. K. (1984). Density-functional theory for time-dependent systems. Physical Review Letters, 52(12), 997.

[32] Casida, M. E. (1995). Time-dependent density functional response theory for molecules. In Recent Advances in Density Functional Methods (Part I), pp. 155–192.

[33] Silverstein, R. M., & Bassler, G. C. (1962). Spectrometric identification of organic compounds. Journal of Chemical Education, 39(11), 546.

[34] Lu, T., & Chen, F. (2012). Multiwfn: A multifunctional wavefunction analyzer. Journal of Computational Chemistry, 33(5), 580–592.

[35] Koch, W., & Holthausen, M. C. (2015). A chemist's guide to density functional theory. John Wiley & Sons.

[36] Shen, L., & Ji, H. F. (2007). Theoretical study on physicochemical properties of curcumin. Spectrochimica Acta Part A: Molecular and Biomolecular Spectroscopy, 67(3–4), 619–623.

[37] Nurhafizah, H., & Rohani, M. S. (2017). Effect of AgCl NPs: Physical, thermal, absorption and luminescence properties. Journal of Molecular Structure, 1137, 150–159.

[38] Nurhafizah, H., & Rohani, M. S. (2017). Effect of AgCl NPs: Physical, thermal, absorption and luminescence properties. Journal of Molecular Structure, 1137, 150–159.

[39] Zabardasti, A., Sharifi-Rad, A., & Kakanejadifard, A. (2015). Interplay between H···O, H···X, X···O and X···X interactions in the complex pairing of formyl halides with hypohalous acids. Spectrochimica Acta Part A: Molecular and Biomolecular Spectroscopy, 151, 746–759.

[40] Feller, D., & Davidson, E. R. (1990). Basis sets for ab initio molecular orbital calculations and intermolecular interactions. Reviews in Computational Chemistry, 1, 1–43.

[41] Hansch, C., Leo, A., & Taft, R. W. (1991). A survey of Hammett substituent constants and resonance and field parameters. Chemical Reviews, 91(2), 165–195.

[42] Mittapalli, S., et al. (2020). Novel solid form of prothioconazole and its crystallographic analysis. Journal of Molecular Structure, 1203, 127406.

[43] Fang, T., Li, Y., & Li, S. (2017). Generalized energy-based fragmentation approach for modeling condensed phase systems. Wiley Interdisciplinary Reviews: Computational Molecular Science, 7(2), e1297.

[44] Billes, F., et al. (2009). Formyl- and acetylindols: Vibrational spectroscopy of an expectably pharmacologically active compound family. Spectrochimica Acta Part A: Molecular and Biomolecular Spectroscopy, 74(5), 1031–1045.

[45] Premkumar, R., et al. (2017). Structural, vibrational spectroscopic and quantum chemical studies on indole-3-carboxaldehyde. AIP Conference Proceedings, 1832(1), 140041.

[46] Ridha, S. M. A., Talib Ghaleb, Z., & Mirdan Ghaleb, A. (2025). Theoretical investigation of the effects of solvents and para-substituents. Revista Mexicana de Física, 71(1).

[47] Ridha, S. M., Ghaleb, Z. T., & Ghaleb, A. M. (2023). The computational investigation of IR and UV-VIS spectra of 2-isopropyl-5-methyl-1,4-benzoquinone using DFT and HF methods. East European Journal of Physics, (1), 197–204.

[48] Asiata, I. O., Kolawole, D. A., & Banjo, S. E. M. I. R. E. (2018). Molecular charge distributions, vibrational frequency and stability studies on 1H-indole-3-carbaldehyde and (Z)-indol-3-ylidenemethanol: DFT approach. Iraqi National Journal of Chemistry, 18(1).